Biosensors and Bioelectronics 306 (2026) 118717

Contents lists available at ScienceDirect

Biosensors and Bioelectronics

journal homepage: www.elsevier.com/locate/bios

High-throughput contractility analysis platform for drug-response evaluation of hiPSC-derived cardiac models based on dynamic frequency conditioning

Paola Casti [a,b], Marcella Brescia [e], Luca Sala [c,d], Arianna Mencattini [a,b], Massimo Mastrangeli [f], Berend J. van Meer [e,g], Eugenio Martinelli [a,b,*]

[a] Department of Electronic Engineering, University of Rome Tor Vergata, Rome, Italy
[b] Interdisciplinary Center for Advanced Studies on Lab-on-Chip and Organ-on-Chip Applications (ICLOC), Via del Politecnico 1, Rome, 00133, Italy
[c] Department of Biotechnology and Biosciences, University of Milano – Bicocca, Milan, Italy
[d] Istituto Auxologico Italiano IRCCS, Center for Cardiac Arrhythmias of Genetic Origin and Laboratory of Cardiovascular Genetics, Milan, Italy
[e] Department of Anatomy & Embryology, Leiden University Medical Center, the Netherlands
[f] Microelectronics Deparment, Delft University of Technology, Delft, the Netherlands
[g] Sync Biosystems, Leiden, the Netherlands

ARTICLE INFO

Keywords:
Contractility evaluation
Experimental pharmacology
Electrical conditioning
Human pluripotent stem cell-derived cardiomyocytes (hiPSC-CMs)
Time-lapse microscopy
Video-based analysis

ABSTRACT

In vitro modelling of cardiac microtissues via human pluripotent stem cell-derived cardiomyocytes (hiPSCs-CMs) holds great promise in experimental pharmacology, especially to improve drug safety and efficacy evaluation. However, the predictive capability of these models is currently hampered by a series of heterogeneity sources mainly related, but not limited to, their immature phenotype. While increased levels of complexity in human-derived models can favor maturation, differences in experimental approaches introduce variability in electrophysiological responses, which is difficult to mitigate. To tackle these aspects, this work proposes a novel measurement strategy in the dynamic frequency regime to induce and analyze multiple operation modes in hiPSC-CMs contraction during drug evaluation. We designed and validated a system for fully automated analysis of cardiac models in a dynamic regime via optical time-lapse microscopy. We show that repeated video-based measurements of the same biological samples in the presence of physical conditioning allow, with appropriate normalization and adjustment operations, accurate estimates of the responses of interest. The analyzed operation modes provided increased representativeness of video-based contractile parameters and reliable trend estimates of concentration-response curves without requiring a high number of biological replicates. In particular, the findings obtained with four benchmark experimental models, including two-dimensional (2D), two-dimensional aligned (2DA), tridimensional microtissues (3D-MTs), and engineered heart tissues (EHTs) in triple cell-type co-culturing, indicate that the proposed approach is effective in drug-response evaluation of four pharmacological compounds with known expected effects and a reference solvent, and offers a promising foundation for the development of high-throughput and robust tools for pharmacological screening.

1. Introduction

Since the advent of human pluripotent stem cell-derived cardiomyocytes (hiPSC-CMs), new possibilities for *in vitro* modelling of cardiac microtissue have been unlocked (Ewoldt et al., 2024; Hwang et al., 2024; Takahashi and Yamanaka, 2006). The benefits of using hiPSC-CMs are remarkable and have been diving the development of bioengineering approaches for 3D constructs and co-cultures of increasing complexity (Novelli et al., 2023; Smith et al., 2017). Advancements in this field aim to more faithfully reproduce the native state of the myocardium (Novelli et al., 2023; Smith et al., 2017) thereby unlocking patient-specific pharmacological testing and regenerative approaches. Existing cardiac experimental models range from standard two-dimensional (2D) cultures to more advanced constructs like micropatterned tissues (Ribeiro et al., 2015), three-dimensional (3D) microtissues (Giacomelli et al., 2017; Richards et al., 2020), engineered

* Corresponding author. Department of Electronic Engineering University of Rome Tor Vergata Via del Politecnico 1, 00133, Roma, Italy.
E-mail address: martinelli@ing.uniroma2.it (E. Martinelli).

https://doi.org/10.1016/j.bios.2026.118717
Received 4 January 2026; Received in revised form 10 April 2026; Accepted 18 April 2026
Available online 22 April 2026

heart tissues (EHTs) (Windt et al., 2023), and heart-on-chips (Visone et al., 2023). By introducing innovative co-culturing protocols (e.g., including hiPSC cardiac fibroblasts, hiPSC-cFBs, and hiPSC endothelial cells, hiPSC-ECs (Windt et al., 2023)) and integrated approaches for external stimulations (e.g., mechanical (Marsano et al., 2016) or electrical (Hinata et al., 2022; van Meer et al., 2019)), novel bioengineered solutions are being developed to increase the physiological relevance of the biological constructs.

The analysis of excitation-contraction dynamics of hiPSC-CMs-based models is pivotal for pharmacological screening and to interpret drug responses in diverse conditions. The most reliable measurement techniques in the field are based, to date, on procedures like patch clamping (Knierim et al., 2024) or the use of voltage-sensitive dyes (Sharma et al., 2018) which, nevertheless, can damage cell membranes or introduce cytotoxic and phototoxic effects. Alternative approaches based on multi-electrode arrays (MEA) can measure hiPSC-CMs' extracellular activity (Caluori et al., 2019; Sala et al., 2017; Tertoolen et al., 2018; Zhang et al., 2022) but are hindered by limited spatial resolution or weak coupling between CMs and electrodes. Video-based contractility analysis (Curci et al., 2026; van Meer et al., 2019; Sala et al., 2018), either via bright-field or phase contrast microscopy in time-lapse (TLM), holds great promise for continuous monitoring of dynamical responses of microtissues with minimal interaction uncertainty or detrimental effects on the biological models under investigation.

However, deriving accurate indicators of hiPSC-CM contractility from TLM videos is highly challenging (Gintant et al., 2020; Sharma et al., 2018) due to multiple sources of uncertainty. Acquisition constraints introduce noise, limited spatio-temporal resolution, distortions, and optical aberrations that might hinder reliable motion analysis (Comes et al., 2019; Curci et al., 2026; Mencattini et al., 2023). Experimental variability further complicates interpretation, as different cell models, culturing strategies, and drug protocols lead to diverse baseline and dynamic responses, preventing the definition of a standard reference (Brescia et al., 2026; Ewoldt et al., 2024). Biological heterogeneity adds another layer of complexity, since hiPSC-CMs exhibit spontaneous, slow, and non-synchronized beating patterns that evolve with maturation and external stimuli (Allegaert et al., 2017). Finally, high-throughput pipelines for estimation of displacement and velocity from TLM videos amplify uncertainty due to limited accuracy, sensitivity to artifacts, and lack of manual tuning (Curci et al., 2026; Sciacchitano, 2019).

High measurement variability necessitates for increasing the number of (costly and time-consuming) biological replicate experiments (Fischer et al., 2019) as well as for robust analysis platforms to support standardization, minimize human-expert interventions and experimental biases, and facilitate comparisons across multiple platforms (Gintant et al., 2020). Modelling approaches of concentration-response curves have been designed to mitigate the effects of non-linearities and heteroscedasticity (Thorin et al., 2010). Anyhow they come with the need for big sample sizes, a higher number of drug concentration levels tested and with mandatory avoidance of missing data that could potentially affect the overall estimates (Hinata et al., 2022; Thorin et al., 2010). External pacing is implemented as a counteraction strategy to reduce the variability caused by the spontaneous beating of hiPSC-CMs (Hinata et al., 2022; van Meer et al., 2019), to promote maturation (Knierim et al., 2024), and to make data comparable across experiments (Zeng et al., 2018). However, the relation between pacing, spontaneous beating rate, and contractility in hiPSCs-CMs remain elusive (van Meer et al., 2019; Zeng et al., 2018). The effects of pacemaking mechanisms on hiPSC-CMs are indeed poorly understood, especially in relation to preexisting cell beating behaviors and related transient responses, time constants, superimpositions and slowly accumulating effects (Zeng et al., 2018).

In this work, hiPSC-based models are regarded as dynamic non-linear systems operating under non-stationary conditions whose responses vary according to multiple ongoing processes and maturation states. Therefore, inspired by the concept of thermal modulation (Lee and Reedy, 1999; Martinelli et al., 2012), where varying operating temperatures provide a clearer and more comprehensive characterization of gas-sensor behaviour, we introduce an analogous form of modulation based on electrical conditioning (external pacing), aimed at improving drug-response evaluation in *in vitro* hiPSC-CM–based models. We hypothesize that the beating patterns exhibited by hiPSC-CMs under multiple pacing frequencies define distinct working points or operating modes that, when jointly analyzed, can characterize the dynamic behavior of the biological system, enabling the extraction of automatic and robust video-based contractility indicators. Following best practice recommendations in the field (Gintant et al., 2020), we designed customized methods that increase the throughput and characterization capabilities of the video analysis pipelines, enabling the exploitation of larger datasets from the same construct in multiple frequency *operating modes*. A schematic representation of the overall pipeline is shown in Fig. 1. Testing is performed with a cumulative drug-administering protocol (four concentration values plus the vehicle control) in the presence of electrical conditioning. At each drug concentration, increasing frequency values are used to explore multiple beating operation modes. TLM videos are acquired at each step and processed through a dedicated analysis pipeline for evaluating drug response. The procedure was substantiated by the establishment of frequency-specific adjustments and appropriate normalizations, which were essential for quantitatively describing the contraction dynamics of individual constructs. We validated the concept using four benchmark hiPSC-CMs-based models, including 2D, 2D-aligned (2DA), 3D MTs, and EHTs in triple cell-type co-culturing, as well as a set of pharmacological compounds with known expected effects.

2. Methods

2.1. Cell co-culture and hiPSCs differentiation

The hPSC line LUMC0020iCTRL-06 hiPSC line (RRID:CVCL_ZA25) (Zhang et al., 2014) used in this study was maintained as previously described (Brandão et al., 2020) in Essential 8™ medium (Thermo Fisher Scientific). The hiPSCs (LUMC0020iCTRL-06) were differentiated into hiPSC-cardiac fibroblasts (cFB) via epicardial progenitor cells (Campostrini et al., 2021), with the few modifications: hiPSCs were seeded at 2.0 x 10^4 cells/cm^2 and 5 μM CHIR99021 was used for mesoderm induction (differentiation day 0 to 2). Medium was then replaced with mBEL +5 μM XAV, 1 μM Retinoic Acid (Sigma Aldrich) and 30 ng/ml BMP4 (R&D Systems) up to day 4. On day 9, the epicardial cells were seeded on fibronectin (5 μg/ml bovine plasma; Sigma Aldrich)-coated wells in mBEL + 10 μM SB431552. When confluent, the epicardial cells were either cryopreserved or further differentiated to cFB on vitronectin-coated plates and culturing for 6 days in mBEL +10 ng/ml FGF2 (R&D Systems). The cFBs were then maintained and expanded in Fibroblast Growth Me.dium 3 (PromoCell), with medium refreshment every 2-3 days.

hiPSC-cardiomyocytes (CM) and hiPSC-endothelial cells (EC), called iCell Cardiomyocytes and iCell endothelial cells were provided as ready to use differentiated cells by Fujifilms (Human Cardiomyocytes | FujiFilm Cellular Dynamics, Inc.). Cells were thawed and cultured according to manufacturer's guidelines.

MT and EHTs were generated as previously described (Giacomelli et al., 2017; Windt et al., 2023), respectively. Both 3D tissues were maintained in mBEL+ 50 ng/ml VEGF and 5 ng/ml FGF2. The different cells were seeded as a mix with the same ratio as the MT and EHTs (70% iCell-CM; 15% iCell-EC; 15% hiPSC-cFB) for the generation of the 2D models (2D and 2DA), in either standard 96 well cell culture plates or in Mimetix® (McKean and Heister, 2017) aligned fibres 3D 96 well plate, respectively, with a total of 6 x 10^4 cells plated per well.

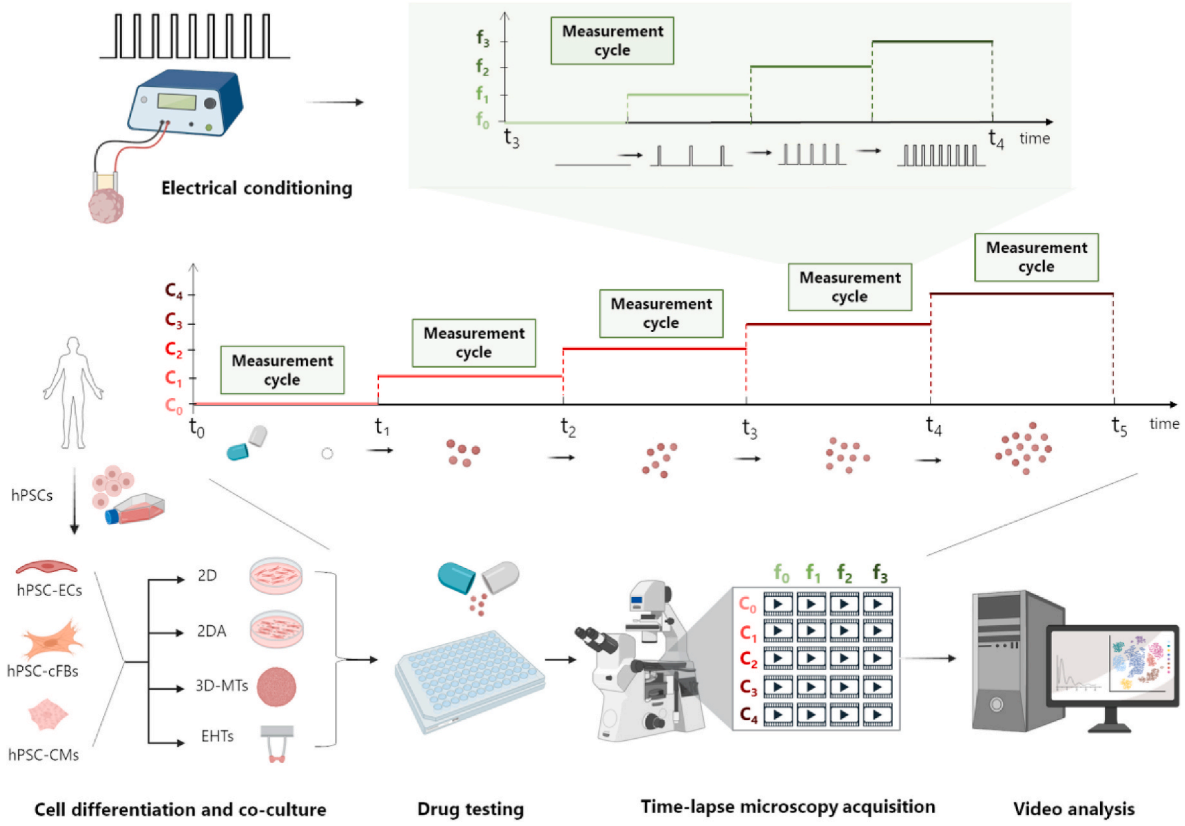

Fig. 1. Schematic representation of the experimental platform for drug-response evaluation in dynamic regime. Triple co-culture of human pluripotent stem cells (hiPSCs), including endothelial cells (ECs), cardiac fibroblasts (cFBs), and cardiomyocytes (CMs) are used in four benchmark cardiac models (2D: two-dimensional monolayers, 2DA: aligned two-dimensional monolayers, 3D-MTs: three-dimensional microtissues, and EHT: engineered heart tissue). Testing is performed with a cumulative drug-administering protocol (four concentration values plus control) in the presence of electrical conditioning. At each drug concentration, increasing frequency values are used to explore multiple beating *operation modes* in spontaneous, 0.5 Hz, 1 Hz, and 2 Hz stimulation conditions, respectively. Time-lapse microscopy videos of ~10 s duration are acquired at each step for a total of 20 videos for each biological sample. Videos are processed through a dedicated analysis pipeline for evaluating drug response. Created in BioRender. Casti, P. (2025) https://BioRender.com/uvjdf6r.

2.2. Experimental setup and measurement protocol

A Nikon Eclipse Ti microscope equipped with a THORLABS CS135MUN Kiralux CMOS camera was fitted with a custom-built environmental chamber that allowed measurements to be performed at 37 °C and 5% CO^2. Electrical conditioning was performed with the apparatus previously described (van Meer et al., 2019; Saleem et al., 2020), with pulses of [5-10] V kept as short as possible (5-10 ms). Spontaneous beating (no pacing) was recorded for 10-20 s before starting with electrical stimulation. Conditioning frequencies were increased in sequence, i.e., 0.5 Hz, 1.0 Hz, and 2.0 Hz, without waiting period in between them. A 10-20 s video was recorded for each condition. The first concentration of the drug was added after recording the baseline contraction of each model and incubated for 30 min before recording. The following concentrations of each compound were added sequentially and also had an incubation time of 30 min before video recording and repeated measurement cycles: [0, 1, 10, 100, 300] nM for *Isoprenaline* (ISO), [0, 10, 100, 300, 1000] nM for *Bay K 8644* (BayK), [0, 3, 10, 30, 300] nM for *Nifedipine* (Nife), [0, 30, 100, 300, 1000] nM for *Blebbistatin* (Bleb), [0, 100, 1000, 10000, 100000] nM for DMSO.

2.3. Microscopy acquisitions and video recordings

Different magnifications were used for the four models: 20x for 2D and 2DA (~0.2 μm/pixel), 10x for MTs (~0.5 μm/pixel), and 4x for EHTs (~1.2 μm/pixel) with varying pixel depths going from 8-bit to 16-bit. A total of 900 TLM videos of 10-20 s duration was analyzed. For each biological model, the TLM data includes five tested compounds at five concentration values (including the baseline, in absence of drug), four stimulation conditions (spontaneous, 0.5 Hz, 1.0 Hz, and 2.0 Hz), and at least two biological replicas: two for 2D (200 TLM videos), MTs (200 TLM videos), and EHTs (200 TLM videos) and three for 2DA (300 TLM videos). Examples of ~10s videos for each biological model are reported as Supplementary Videos1-4.

Supplementary video related to this article can be found at https://doi.org/10.1016/j.bios.2026.118717

2.4. Video-based analysis workflow

A flowchart of the proposed pipeline for video-based analysis of hiPSC-derived models is shown in Fig. 2 and described in the following.

2.4.1. Pre-processing

All frames are *standardized* to make videos consistent in terms of spatial resolution and pixel depths. To be robust at variations in pixel depths and anomalous pixel values, the bottom and top 1% of all pixel values are saturated and intermediate values are linearly mapped in [0, 1] via histogram stretching (Rafael and Gonzalez, 2018). All frames from videos acquired at different magnifications or settings are resized to the same spatial resolution of 0.5 μm/pixel via bicubic interpolation (upsampled or downsampled according to the magnification), and quantized to the same pixel-depth of 8 bit for computational efficiency. Contrast-limited adaptive histogram equalization (CLAHE) (Zuiderveld, 1994) with tiles of size [10x10] μm and 2^8 bins is applied, frame by frame, to locally match intensity histograms to uniform distributions and facilitate displacement analysis. This step is also pivotal to ensure

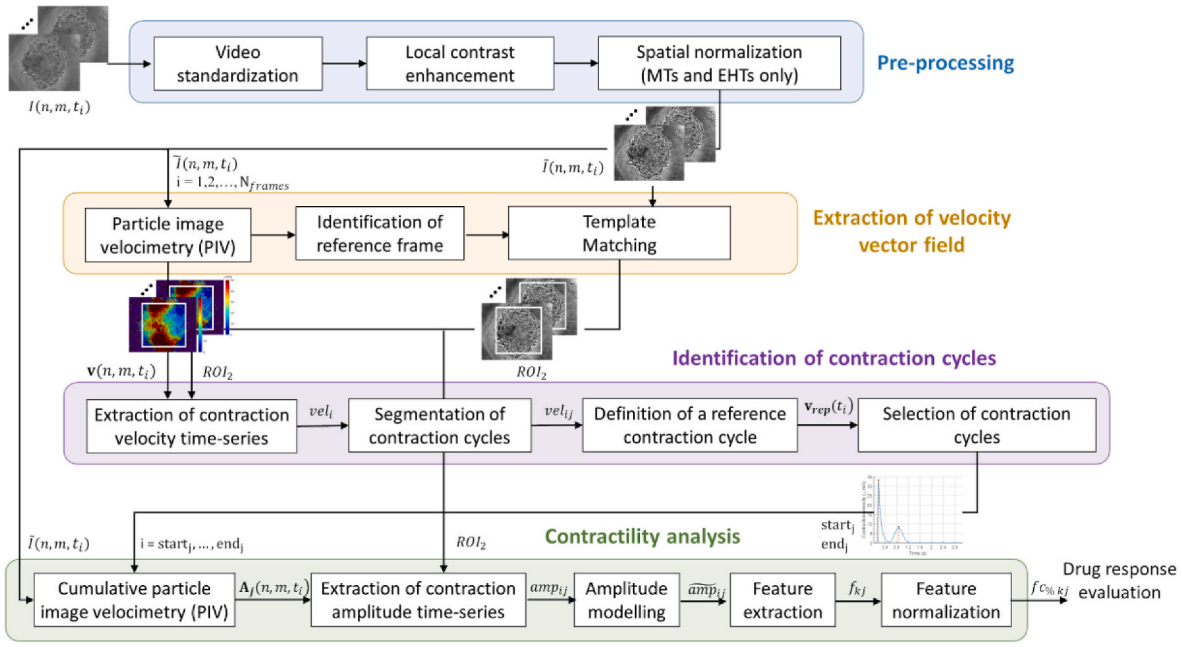

Fig. 2. Methodological steps for the analysis of CM contractility in time-lapse microscopy videos of hiPSCs-based models and drug-response evaluation. Time-lapse microscopy videos are analyzed via a dedicated pipeline, including pre-processing, extraction of velocity vector field, identification of contraction cycles, contractility analysis and drug response evaluation based on known contractility indicators. Standardization and normalization procedures are present to ensure consistency and robustness to sources of experimental heterogeneity.

that illumination variations are compensated. Examples of preprocessed frames for each model are shown in Fig. 3.

2.4.2. Spatial normalization of the 3D constructs

For the case of 3D MTs and EHTs, a segmentation phase is added to the workflow to derive squared regions of interests excluding the background and centered at the centroid of the segmented microtissues. Spatial normalization (see Fig. 2) is pivotal for reducing unnecessary computational costs, increasing the signal-to-noise ratio of the displacement and velocity signals, and for ensuring consistency of the analyzed regions over time, i.e., stability of the observation window. The microtissues are segmented and aligned based on a Segment Anything Model (SAM) (Kirillov et al., 2023), as described in Supplementary Materials.

2.4.3. Contraction velocity estimation

Consecutive pre-processed frames, $\widetilde{I}(n,m,t_i)$ and $\widetilde{I}(n,m,t_{i+1})$, with $n = 1,2,\ldots,N$, $m = 1,2,\ldots,M$, $i = 1,2,\ldots,N_{frames}-1$, are analyzed via Particle Image Velocimetry (PIV), PIVlab (Thielicke and Sonntag, 2021). The core of the algorithm, designed by Thielicke and Sonntag, implements ensemble cross-correlation with squared interrogation windows and uniform spatial sampling (Cartesian grid) over the whole frames. Such an approach has been shown to be effective in micron-resolution displacement estimates and with particle-like microstructures, which are reminiscent of hiPSC-CMs (Thielicke and Sonntag, 2021). Preliminary tests have been performed to define the main settings for the analysis: two passes interrogation with 50% overlap and windows of sizes of [64 x 64] pixels ([32 x 32] μm) and [32 x 32] pixels ([16 x 16] μm). The velocity values derived via PIV in correspondence of the subset of interrogation windows with known resolution can be expressed in μm/s. To improve computational efficiency, cross-correlation is performed in the frequency domain using the discrete Fourier transform (DFT), followed by B-spline interpolation. The obtained velocity fields are averaged spatially and smoothed with moving average filtering. Finally, subpixel precision is achieved by fitting a one-dimensional Gaussian function to the intensity distribution of the correlation matrix for both axes independently to derive the 2D vector field, $\mathbf{v}(n,m,t_i)$, with $n = 1,2,\ldots,N$, $m = 1,2,\ldots,M$, $i = 1,2,\ldots,N_{frames}-1$, and components $v_x(n,m,t_i)$ and $v_y(n,m,t_i)$, along the x and y directions, respectively (Thielicke and Sonntag, 2021) (see Fig. 2).

Average velocity time series, vel_i, sampled at time t_i, are computed from the absolute values of $v_x(n,m,t_i)$ and $v_y(n,m,t_i)$ in the automatically selected Regions of Interests (ROIs) as:

$$vel_i = \sqrt{\left[\underset{n,m\in ROI}{\text{mean}}\left(|v_x(n,m,t_i)|\right)^2 + \underset{n,m\in ROI}{\text{mean}}\left(\left|v_y(n,m,t_i)\right|\right)^2\right]}. \quad (1)$$

with $i = 1,2,\ldots,N_{frames}-1$

Borders of 32 pixels (16 μm) at each side of the ROI are excluded from the mean computation to avoid border effects. Motion artifacts are detected as velocity values discarding the corresponding median signal more than two times its standard deviation, i.e., including ~95% of data points. Values of velocityin correspondence of the artifacts are substituted with the average value of the two adjacent frames. Finally, signals are low-pass filtered with a passband frequency of 20 Hz.

2.4.4. Spatial matching and selection of contraction cycles

The positioning of the same biological entity (monolayer or microtissue) in the field of view can vary over the course of the experiment due to electrical conditioning, drug administration, or human interventions, such as in the case of bubble removal. To achieve robustness to motion drifts, corresponding ROIs in subsequent experimental conditions are determined, in a consecutive manner, via template matching using a cross-correlation approach (Chen et al., 2007). Velocity time-series obtained by averaging over the updated ROIs, i.e., ROI_2 (shown in Fig. 3), are used to refine the analysis and finally segment the contraction cycles (see Supplementary Materials and Fig. 2). Given the detected starting and ending frames at time t_{start_j} and t_{end_j}, respectively, the average velocity time-series of the j^{th} contraction cycle, with $j \in J_0$, is given by

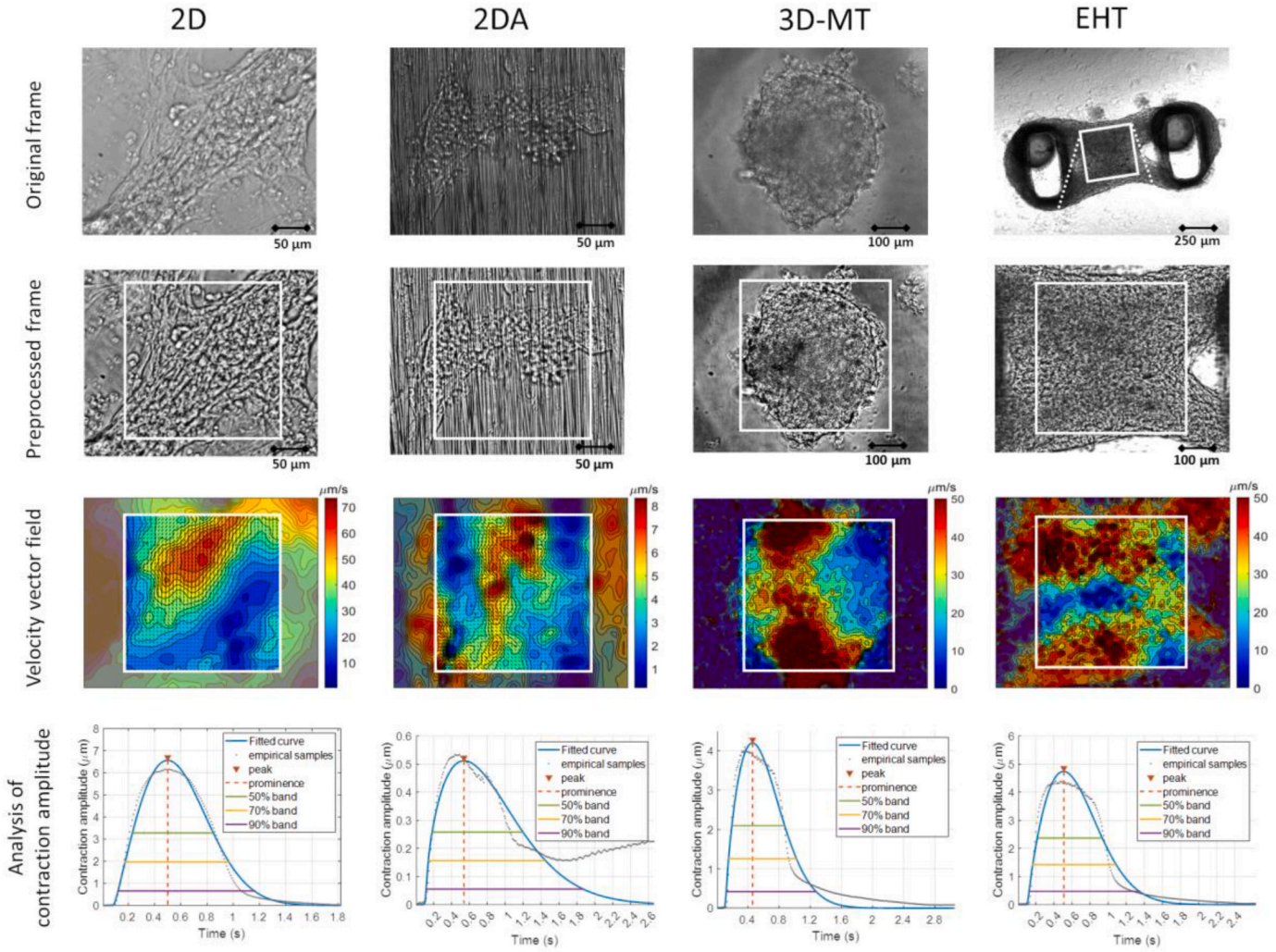

Fig. 3. Intermediate results for case examples of four hiPSCs-based models (2D, 2DA, 3D-MT, and EHT) in baseline conditions. Original frames, preprocessed frames and corresponding extracted regions of interests (ROI_2), velocity vector fields extracted in correspondence of a peak of contraction in the velocity time series, vel_i, results of the analysis of the contraction amplitude with empirical samples, fitted Weibull-shaped functions, detected peaks, prominence, and bands at the 90%, 70%, and 50% obtained with the fitted curves.

$$vel_{ij} = \sqrt{\left[\underset{n,m\in ROI_2}{\text{mean}}\left(|v_x(n,m,t_i)|\right)^2 + \underset{n,m\in ROI_2}{\text{mean}}\left(|v_y(n,m,t_i)|\right)^2\right]} \text{ with i} = \text{start}_j, \text{start}_j + 1, \ldots, \text{end}_j, j \epsilon J_0 \tag{2}$$

To increase robustness to aftercontractions and irregular beating patterns, for each video, a representative contraction cycle is computed as $\mathbf{v}_{rep}(t_i) = \underset{j}{\text{median}}(vel_{ij})$ used to select subsets of contractions cycles based on signals similarity ($\rho > 0.75$). The duration, T, of the representative cycle is set as the median of the peak-to-peak distances of the contraction peaks in vel_i. Additional details on spatial matching and procedures to recover abnormal/twitching contractions are reported in the Supplementary Materials.

2.4.5. Cumulative displacements estimation

Given the j^{th} contraction cycle, with $j \epsilon J$, extracted from the video $v_{rp}(c_i) \in V$, relative to the r^{th} replica at the p^{th} stimulation condition and i^{th} drug concentration, PIV is used to estimate the amplitude of contraction, $\mathbf{A_j}(n,m,t_i)$, with $n = 1,2, \ldots,1024$, $m = 1,2, \ldots,1280$, t_i, with $i = \text{start}_j, \text{start}_j + 1, \ldots, \text{end}_j$, and components $A_x(n,m,t_i)$ and $A_y(n,m,t_i)$, along the x and y directions, respectively, with reference to the undeformed configuration. In this case, displacements between pairs of frames at time t_i and t_{start_j} are considered to quantify cumulative displacements (or local deformations) via PIV. The so-derived components of the displacement fields are used to determine the average contraction amplitude time series for the j^{th} contraction cycle, amp_{ij}, as

$$amp_{ij} = \sqrt{\left[\underset{n,m\in ROI_2}{\text{mean}}\left(|A_x(n,m,t_i)|\right)^2 + \underset{n,m\in ROI_2}{\text{mean}}\left(|A_y(n,m,t_i)|\right)^2\right]} \quad \text{with i} = \text{start}_j + 1, \text{start}_j + 2, \ldots, \text{end}_j, j \in J \tag{3}$$

2.4.6. Amplitude modelling

Each contraction amplitude time series of duration T relative to a single contraction cycle is modelled with a 4-parameters Weibull-shaped function defined as

$$\widetilde{amp}_{ij} = \begin{cases} a\frac{\beta}{\eta}\frac{(t_i-\gamma)^{\beta-1}}{\eta} e^{-\left(\frac{t_i-\gamma}{\eta}\right)^{\beta}} & t_i \in (\gamma, T) \\ 0 & t_i \le \gamma | t_i \ge T. \end{cases} \text{ with i} = \text{start}_j + 1, \text{start}_j + 2, \ldots \text{end}_j, j \in J \tag{4}$$

with a the amplitude parameter, $\beta > 1$ the shape parameter, $\eta > 1$ the scale parameter, and γ the location, or threshold, parameter. The choice

of fitting the PIV-derived signals to a model in a least-squares sense is motivated by the need of being robust to the presence of extra-beats or noise. The model in Eq. (4) allows for proper modelling of right-skewed data (with β), zero-adjustment of the initial and final average amplitude values of each contraction cycle (with γ and constraints in 0), mitigation of errors related to the identification of the contraction start (with γ), and flexibility in terms of peak and duration of the contraction (with a and β, respectively). Examples of the fitted curves are shown in Fig. 3. The first derivatives, $\widetilde{amp}'_{ij}$, of the obtained time series are computed as central finite differences and used, together with $\widetilde{amp}_{ij}$, for feature extraction. In particular, each descriptor is extracted from the single lobe of $\widetilde{amp}_{ij}$ and from the two lobes relative to the contraction and relaxation phases of $\widetilde{amp}'_{ij}$, for a total of 27 features.

2.4.7. Extraction of contractility indicators

Concentration-response curves were derived for a set of contractility indicators that are mostly used in the field. A summary of the descriptors and their definitions is reported in Table 1. For each contraction cycle, the same descriptors are extracted from the peak of the contraction amplitude signals (as shown in Fig. 3) and from the two peaks of the contraction and relaxation phases of the velocity signals in all experimental conditions, including repeated rounds, different electrical stimulation frequencies, and drug concentrations. Contraction amplitude peak and contraction duration, in particular, are used to validate the proposed approach based on the expected effects of the drugs under analysis in four cell configurations or biological models.

2.4.8. Normalization

For each biological model, normalization of the descriptors with reference to the control condition at the same stimulation frequency was devised to warrant invariance to individual properties of the biological replicas and response variations related to the frequency of stimulation. Since electrical conditioning and drug exposure are performed in a cumulative and interlaced modality (see Fig. 1), the responses at different stimulation conditions must be considered together. This assumption is motivated by the presence of combined (non-linear) effects (drug/conditioning), including memory effects, which do not allow, in this experimental scenario, for drug-response evaluation frequency by frequency. Hence, responses at different stimulation conditions are considered as *working points* or *operating modes* of the same biological entity. Therefore, each descriptor, $f_{kjrs}(c_l)$, with $k = 1, 2, \ldots, 27$ features obtained at drug concentration c_l, with $l = 0, 1, \ldots, 4$, with the s^{th} conditioning condition, $s \in \{spontaneous, 0.5\,Hz, 1\,Hz, 2\,Hz\}$, in the r^{th} replica, $r \in \{1, 2\}$, from the j^{th} contraction cycle, $j \in J$, is normalized with reference to the corresponding baselines at c_0, i.e., in absence of drug, at the same replica, same conditioning condition, as follows

$$f_{\%\,kjrs}(c_l) = \left\{ \frac{f_{kjrs}(c_l)}{\underset{j}{\text{mean}}\left[f_{kjrs}(c_0)\right]} \right\} x100 \tag{5}$$

and expressed in terms of relative percentage variations from the 100 % level. The baseline response is obtained as the average of the descriptor values over multiple contraction cycles for the corresponding replica and stimulation conditions.

2.4.9. DMSO adjustment

To adjust the indicators so that they provide null percentage variations in the presence of the solvent only and along the overall experimental procedure, all the concentration-responses were corrected for the corresponding DMSO baseline, $f^{DMSO}_{\%\,kjrs}(c_l)$. In this case, the average percentage gap measured in presence of DMSO at drug concentration c_l, $\Delta f^{DMSO}_{\%k}(c_l) = \underset{j,r,s}{\text{mean}}\left[f^{DMSO}_{\%\,kjrs}(c_l)\right] - 100\%$, are considered as the background indication, or the zero-response condition, for the correction, as

$$\begin{aligned} fc_{\%\,kjrs}(c_l) &= f_{\%\,kjrs}(c_l) - \Delta f^{DMSO}_{\%k}(c_l) = f_{\%\,kjrs}(c_l) \\ &\quad - \left(\underset{j,r,s}{\text{mean}}\left[f^{DMSO}_{\%\,kjrs}(c_l)\right] - 100\% \right) \quad \text{with } l = 0, 1, \ldots, 4 \end{aligned} \tag{6}$$

This step is pivotal to ensure, as possible, that the effects of the analyzed compounds in dynamic regime are isolated from the effects of the solvent or from cumulative-memory effects related to the experimental procedures. When DMSO responses at c_l are not available, $f^{DMSO}_{\%\,kjrs}(c_l)$ is derived via linear interpolation of available values at adjacent concentrations, given that the available concentration values were not sufficient to justify a sigmoidal fitting. Although samples independence could not be assumed by experimental design, the extraction of contractility descriptors relative to dynamically conditioned beating patterns and their formulation subsequent to dedicated processing steps (i.e., Weibull-modelling corrections, normalization, and adjustment) support our choice of treating them as pseudo-exchangeable measurements (Mikosch and Kallenberg, 1998). Therefore, feature values relative to multiple contraction cycles and multiple frequency conditioning are considered as pseudo-independent operation modes in a dynamic conditioning regime and averaged in the concentration-response evaluation.

Table 1
Summary of contractility parameters.

#	Feature Name	Variable Name	Description
1	**Contraction Duration**	cd90	Time rise from the 90% of the peak height
2	**Relaxation Duration**	rd90	Time fall to the 90% of the peak height
3	**50% Duration**	CD50	Duration (band width) at 50% of the peak height
4	**70% Duration**	CD70	Duration (band width) at 70% of the peak height
5	**90% Duration**	CD90	Duration (band width) at 90% of the peak height
6	**100% Duration**	CD100	Total duration
7	**Amplitude peak**	AMP	Maximum value
8	**Rise Slew Rate**	RSR	Maximum rate of increase (during rise)
9	**Fall Slew Rate**	FSR	Maximum rate of decrease (during fall)

* each descriptor is extracted from the single lobe of the fitted contraction amplitude signal, $\widetilde{amp}_{ij}$, and from the two lobes relative to the contraction and relaxation phases of its derivative, $\widetilde{amp}'_{ij}$, respectively, for a total of 27 features. Note that after fitting, the baseline of each lobe is always zero.

2.5. Statistical analysis

For each descriptor, sample points outside the 5th and 95th percentiles of data relative to individual biological replicas at a given drug concentration are detected and replaced via linear interpolation without altering the overall sample size. For the four drugs, multiple comparisons of the treatment effects with the control group (absence of treatment, c = 0 nM) are performed with the Shirley-Williams (S-W) test (Hamada, 2018). In addition, Jonckheere-Terpstra (J-T) test was performed to determine the significance of the trend in the obtained dose-response curves (Hamada, 2018).

2.6. Multivariate modelling

Drug responses obtained under multiple experimental conditions were evaluated in multivariate spaces both at the level of individual biological models and globally. The most discriminative descriptors were automatically selected with a wrapper-type feature selection

approach and linear discriminant analysis (LDA) in K-fold (K = 4) cross-validation (CV) using the last two drug concentration values for each compound. The obtained average (and standard deviation) accuracy relative to the automatic discrimination of the compounds was assessed in a five-class scenario, including DMSO. Principal Component Analysis (PCA) was then used for exploratory analysis and visualization. (Bishop, 2006).

3. Results

3.1. Comparative analysis

As a preliminary step, we compared the contractility responses obtained with a correlation-based approach based on PIVlab (Thielicke and Sonntag, 2021), with MUSCLEMOTION (MM) (Sala et al., 2018) and with BeatProfiler (BP) (Kim et al., 2024), which were chosen as the benchmark methods for high-throughput video-based analysis of hiPSC-derived cardiac models. Given the absence of a reference ground-truth for the real experimental data, we used artificially generated videos with real-like morphology and known displacement fields (Curci et al., 2026) in baseline condition first (Supplementary Videos 5 and 6, respectively), confirming the capability of all tools of extracting the contraction dynamic from TLM videos. To test the sensitivity to known variations, and so the accuracy in relative terms with reference to a baseline, we generated a set of five artificial videos of beating cardiomyocytes with increasing simulated variations in contraction amplitude (increasing percentage variations of the average peak amplitude up to 50% (Visone et al., 2023)) obtained at fixed contraction periods (Supplementary Videos 7-11). The results of comparative analysis (reported in Section C of Supplementary Materials and discussed in Section 4) motivates the need for tailoring an automatic system based on cross-correlation to derive contractility measurements in dynamic conditions, which was addressed in this work.

Supplementary video related to this article can be found at https://doi.org/10.1016/j.bios.2026.118717

3.2. Concentration-response evaluation

The overall proposed analysis pipeline was tested on four drug compounds (plus DMSO) with known expected effects, and based on the biological models most widely used in the literature, i.e., 2D monolayers, 2DA monolayers, 3D-MTs, and EHTs. The biological representativeness was furtherly enhanced by the presence of co-cultures with three cell types including, in addition to hiPSC-derived CMs, ECs and cFBs. For each experimental scenario, different sources of variability in dynamic conditions have been considered: 1) the temporal variability, with the presence of multiple contraction beats, 2) the biological variability, with the presence of multiple biological replicates ($n \geq 2$), and 3) the dynamic variability, with the presence of multiple operation modes (at different conditioning frequencies). A total of 38,955 contraction samples (i.e., single analyzed contractions) were extracted from the TLM videos. From the initial set of 900 TLM videos, 805 (~90%) were completely processed and analyzed in a high-throughput modality. A small subset of videos was automatically discarded by the system, e.g., samples in absence of beating or with too low signal to noise ratio, including 7, 19, 19, 18, and 32 videos at baseline, at the second, third, fourth, and highest tested concentrations, respectively, the latter corresponding to conditions under which samples are expected to lose their contractility patterns. The extracted data corresponds to 865 contraction samples (relative to 147 TLM videos) for *Isoprenaline*, 769 contraction samples (relative to 161 TLM videos) for *Bay K 8644*, 1037 contraction samples (relative to 162 TLM videos) for *Nifedipine*, 964 contraction samples for *Blebbistatin* (relative to 186 TLM videos), and 679 contraction samples for DMSO (relative to 149 videos).

To objectively compare model performance, we quantified drug-induced effects in terms of:

1. Percentage variation (mean ± SD) relative to baseline (concentration-response curves);
2. Statistical significance (single-concentration, S-W, and trend, J-T, significance tests, $p < 0.01$);
3. Concentration threshold at which significant responses first appear.

Average concentration-responses on the beating-frequency values (in Hz) are shown in Fig. S4 of the Supplementary Material. Values were obtained as the reciprocal of the contraction cycle duration (in s), averaged over all the detected beats from the same video, i.e., $\underset{j}{\text{mean}}\left[1/f_{(k=RR)jrs}(c_l)\right]$. The average number of videos analyzed for each concentration value is also indicated.

The average concentration-responses obtained with contraction duration (CD90) and contraction amplitude peak (AMP) are shown in Fig. 4 a) and b), respectively. Results are reported for the five analyzed compounds (in different rows) and four biological models (in different columns). The percentage variation of the descriptor is reported as function of the concentration value (Log(1+c), with c in nM). The logarithmic scale with base 10 was chosen to better represent the extent of concentration values. The results obtained with other indicators are reported in the Supplementary Materials. Statistically significant ($p < 0.05$, *, $p < 0.01$, **) drug effects with reference to the control group are indicated for all the concentration-responses. The asterisks in correspondence of the treatment effect at single concentration values are shown only in the presence of concomitant rejection of the null hypothesis of the Jonckheere-Terpstra test, i.e., in the presence of the expected significant trend of the responses at increasing concentration values.

With reference to CD90 (see Fig. 4a), statistically significant trends (T.S. $p < 0.01$), in accordance with the expected effects, were obtained for ISO, BayK, Nif, and Bleb in all investigated models (Table S1). However, clear differences emerged in terms of effect magnitude and concentration-dependent sensitivity. EHT models exhibited the largest significant average percentage variations, going from −7% at 10 nM for ISO to +66% at 100 nM for BayK (Table S2). Moreover, 2D and EHT were the only configurations achieving statistically significant responses (S-W $p < 0.01$) starting from the second tested concentration (C2) across all compounds, indicating lower detection thresholds. Compared to 2D cultures, EHTs showed consistently larger variations, showing higher sensitivity to positive inotropes in terms of CD90. In contrast, MTs exhibited attenuation of the response at higher concentrations (particularly for ISO and BayK), suggesting reduced dose–response stability.

In terms of AMP (see Fig. 4b), most of the trends were consistent with the expected pharmacology (See Table S1). MTs exhibited the highest sensitivity to positive inotropes, with statistically significant increases observed at the lowest tested concentrations (+34% at 1 nM for ISO and +42% at 3 nM for BayK). This indicates superior early detection capability for positive amplitude effects. Although the investigated EHT configuration did not fully reproduce the expected BayK trend, a substantial increase of +57% at 10 nM was observed. Negative inotropic trends (Nif and Bleb) were statistically significant across models, with lower p-values in 2D cultures. To further clarify model robustness, Fig. S9 reports examples obtained under single-frequency pacing showing low statistical power, high variability, and p-values >0.05. These observations demonstrate reduced dose–response stability under simplified experimental conditions and provide additional support for the proposed multi-condition analytical framework.

The other average responses, reported in the Supplementary Materials, also exhibit consistent trends, depending on the model and drug compounds, providing additional indications of the kinematic and dynamic profiles of hiPSC-CMs-based models.

3.3. Discriminant capability of the tested compounds

The discriminant capabilities of the derived descriptors with

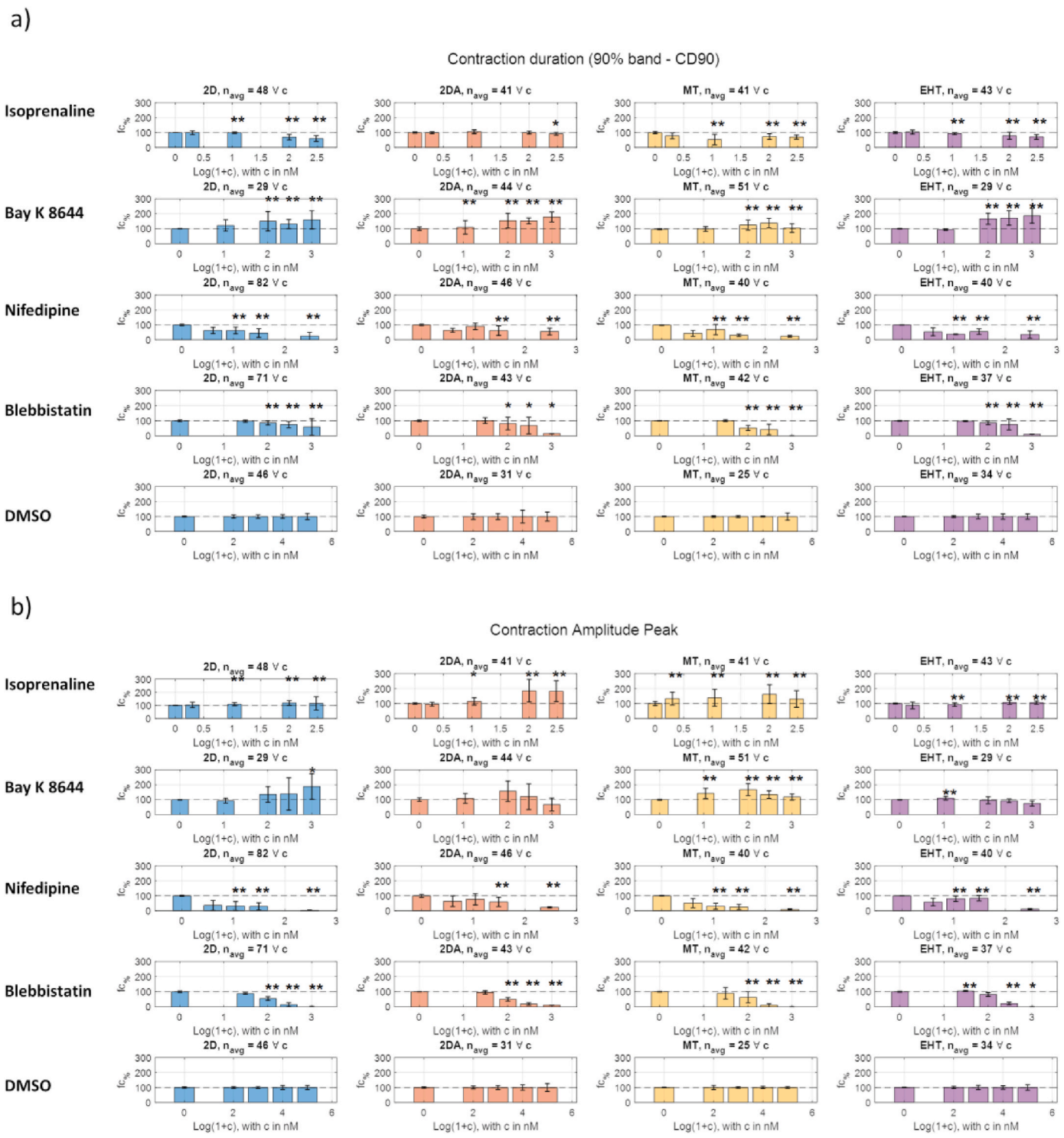

Fig. 4. Average (and standard deviation) concentration responses obtained with four benchmark biological models (2D, 2DA, MT, EHT) and four drug compounds (plus DMSO condition) relative to a) contraction duration (CD90) and b) contraction amplitude peak (AMP). The number of average samples, n_{avg}, per concentration is reported for each analyzed scenario, taking into account 1) the experimental repeatability, with multiple contraction beats, 2) the biological variability, with multiple biological replicates ($n \geq 2$), and 3) the dynamic variability with multiple operation modes.

reference to the analyzed compounds were evaluated in a five-class scenario. Average (and standard deviation) accuracy values of 0.86 (0.01), 0.72 (0.04), 0.80 (0.05), and 0.75 (0.02) were obtained with LDA on 2D, 2DA, MTs, and EHTs, respectively, using automatically selected contractility indicators. In Fig. 5, corresponding PCA plots are shown, for individual models and, globally, for all models. The color codes indicate the five compounds in Fig. 5a–e and the biological models, in Fig. 5f.

4. Discussion

One of the main challenges in in vitro models of hiPSC-CMs is the heterogeneity of their beating patterns. This variability depends on the differentiation batch, experimental platform, co-culture conditions, and,

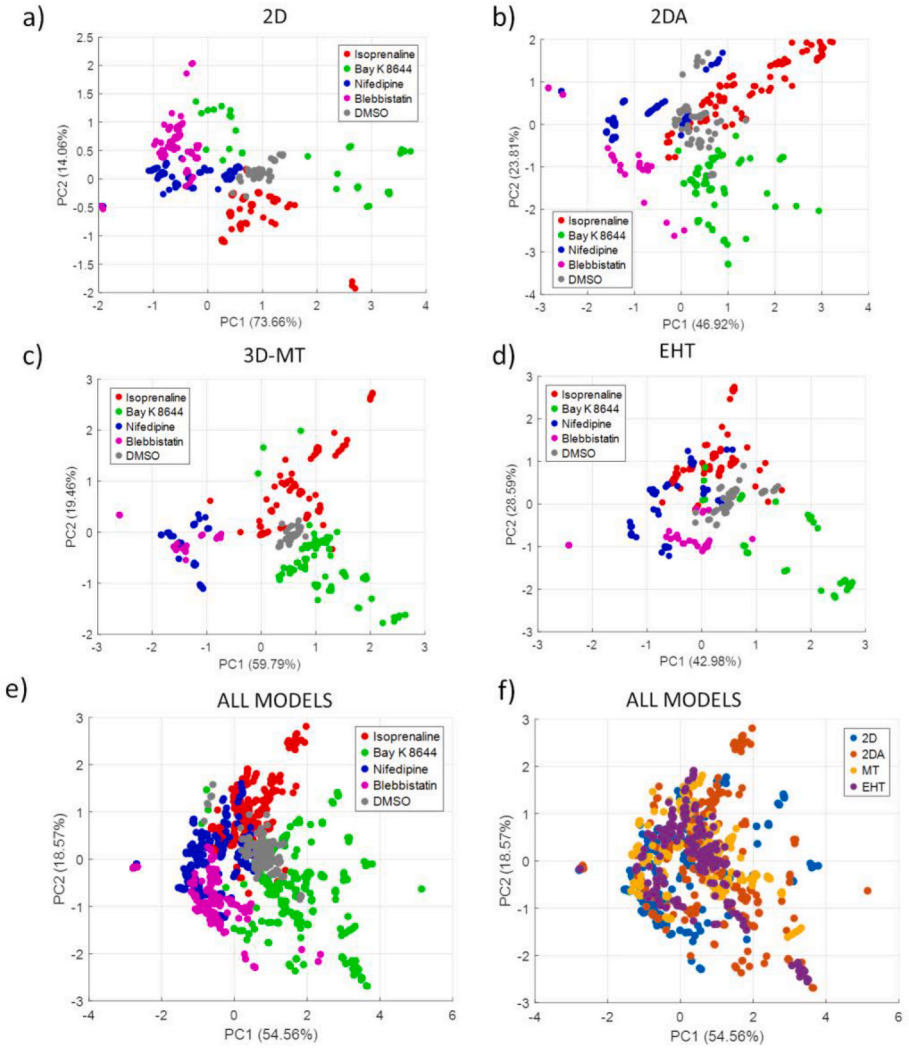

Fig. 5. PCA plots obtained with selected contractility indicators and the four benchmark models. The colour code indicates the drug compounds (a-e) or the biological models (f). Data is relative to the last two drug concentration values evaluated on 501 samples (2D), 362 samples (2DA), 352 samples (MTs); 333 samples (EHTs), and a total of 1548 samples (ALL MODELS). (For interpretation of the references to colour in this figure legend, the reader is referred to the Web version of this article.)

most importantly, their level of electrophysiological maturation. In vitro hiPSC-CMs show spontaneous and evolving beating rates, and their responses to external stimuli remain only partially understood (Hinata et al., 2022).

To standardize contractility analysis, fixed electrical pacing is typically applied to impose a controlled rhythm and improve the reliability of concentration–response studies. However, as in clinical pacemaking, the ability of cells to follow imposed pacing depends on their physiological state and intrinsic beating behavior (Zeng et al., 2018). Cells do not always achieve the desired frequency, particularly within limited experimental timeframes. Without automatic sensing or closed-loop feedback, variability in response dynamics reduces throughput and requires continuous manual adjustment of stimulation parameters (Guerrelli et al., 2024). Even when frequency stabilization is achieved, functional performance may still differ due to co-culture composition and phenotypic heterogeneity (Tadevosyan et al., 2026).

Additional variability may arise from experimental procedures (Guerrelli et al., 2024), electronic fluctuations (Swerdlow et al., 2020), or environmental electromagnetic interference (Pinski and Richard, 2000), all of which can hamper steady-state conditions. Mechanical stimulation has been proposed as an alternative strategy to improve electrophysiological homogeneity (Marsano et al., 2016; Visone et al., 2023). Combinations of repeated measurements and modelling approaches of concentration-response curves have been proposed in the literature to mitigate the effects of non-linearities (Batista et al., 2019; Thorin et al., 2010). However, these alternative statistical frameworks typically require larger sample sizes, a greater number of tested drug concentration levels, and stricter handling of missing data, as these factors can significantly influence the reliability of the overall estimates (Hinata et al., 2022; Thorin et al., 2010).

In this work, we explore dynamic electrical stimulation as a conditioning strategy to enhance data representativeness in video-based contractility analysis. By applying increasing pacing frequencies in the range 0.5–2 Hz, multiple operational modes can be obtained from each biological replicate at a given drug concentration. Compared to spontaneous activity alone, this approach provides multiple measurements from the same biological entity, increasing sample size and representativeness at reduced cost, effectively creating a virtual cohort. Measurements were acquired across dynamically distinct states, which were considered as separate realizations of the system's response. While strict independence cannot be assumed, the so derived observations were treated as pseudo-independent based on the notion that the hiPSC-CMs functional outputs change with the beat rate and so is their drug responsiveness (Garcia et al., 2025). This choice is further supported by

recent evidence in the literature (Guerrelli et al., 2024) demonstrating the significant impact of equilibration duration and pacing parameters on hiPSC-CMs electrophysiology and their influence on experimental reproducibility. Moreover, we have observed that over the course of the experiment, cells and biological models under investigation underwent positioning changes and displacements that make them visually and morphologically different, in the field of view, from their initial states at the baseline. Changes in appearance were paired with non-linear changes happening over time in CMs contractility and combined effects of intrinsic automaticity and of external pacing. These aspects posed substantial challenges from an analytical perspective, motivating the need for the design of an ad-hoc measurement approach, capable of handling the variability arising from dynamic electrical stimulation combined with interleaved drug administration.

Statistically significant CD90 trends were observed for all compounds across models, consistent with their expected inotropic effects. ISO reduced contraction duration (negative CD90 trend) in all models via β_1-adrenergic receptor activation, whereas BayK prolonged contraction due to sustained cytosolic Ca^{2+} transients. Nif and Bleb also showed negative CD90 trends, in line with their negative inotropic action.

AMP increased with concentration for positive inotropes (ISO, BayK) and decreased for negative inotropes (Nif, Bleb), as expected. However, positive inotropic effects on AMP diminished at higher concentrations, particularly for BayK in 2DA, MTs, and EHTs. In EHTs, the expected AMP increase lost its statistical significance, possibly due to the pillar stiffness used in this study, which may counterbalance force enhancement (Gokhan et al., 2024; Windt et al., 2023). Unlike other studies (Kim et al., 2024; Sala et al., 2018), the pillars were designed to provide mechanical load rather than enable deflection-based force measurements (see Supplementary Video S4). This configuration is consistent with a simulated increased afterload condition.

The AMP reduction observed at the highest concentrations in 3D MTs and EHTs with ISO, and in 2DA, MTs, and EHTs with BayK, may indicate arrhythmogenic events and spatially discordant alternans (SDA), which are expected at these concentrations (Xie and Weiss, 2009). These findings support the idea that structurally advanced 3D models better capture cardiac complexity and improve toxicological reliability. Aligned electrospun fibers in 2DA models, for example, should promote anisotropic cell organization that better recapitulates the structural arrangement of native myocardium compared to conventional 2D monolayers and have been shown to improve hiPSC-CM maturation (Khan et al., 2015; Robinson et al., 2021).

Negative inotropic trends were consistent across models in terms of AMP, while DMSO showed stable responses due to the normalization procedure (see Fig. 4). As shown in Fig. S9, single-frequency pacing can yield unstable (absence of trends, with $p > 0.05$) or even opposite responses (with $p < 0.01$ in the opposite direction, as for the case of increased CD90 with Nife), because of limited sample size and data heterogeneity. In contrast, the proposed high-throughput approach restores statistical power and improves the reliability of video-based contractility metrics in models including hiPSC-CM, hPSC-cFBs, and hPSC-ECs without increasing biological replicates or imposing stricter experimental constraints.

The extracted descriptors show good discriminative ability in a five-class classification task using the two highest drug concentrations. The best overall classification performance was obtained with 2D models. Although EHTs and MTs may be more sensitive for specific descriptors, 2D cultures provide better global separability among compounds.

PCA was performed to elucidate, in 2D-space representations, the multivariate information content brought by the contractility descriptors and their capability not only to quantify the dynamic responses of hiPSC-derived cardiac models but also to differentiate among different pharmacological compounds or experimental models. The score plots in Fig. 5a–e shows clustering of the five compounds, with positive and negative inotropes positioned close to each other and the solvent located between them. Importantly, Fig. 5f indicates that samples are not clustered by model type, revealing shared dynamic response patterns across configurations captured by the proposed measurement strategy. Nevertheless, partial overlap between samples suggests model-specific effects and highlights the unique contributions of each biological system.

Overall, these findings underscore the intrinsic limitations of individual models and support a complementary multi-model approach for comprehensive drug characterization. Different platforms optimize different criteria: sensitivity (EHTs, MTs) versus statistical robustness and classification separability (2D). Combining models therefore improves pharmacological assessment compared to single-model analysis.

To date, MM (Sala et al., 2018) and the more recent BeatProfiler (Kim et al., 2024) represent state-of-the-art tools to deal with the analysis of CMs contractility in TLM videos in an automated and non-invasive manner. They both possess the invaluable advantage of being user-friendly and applicable to different experimental models and data modalities, allowing for high-throughput investigations, as compared with other existing methods requiring manual tuning or dedicated training. BeatProfiler extends the functionalities of MM with the possibility of analyzing calcium transients, extracting binary masks via deep learning approaches, segmenting individual beats, and classifying conditions of interests based on machine learning techniques.

The comparative analysis reported in Supplementary Materials, proved increased accuracy in the displacement measurements based on a cross-correlation approach, i.e., PIVlab (Thielicke and Sonntag, 2021). The improvements are evident with reference to the known true values of the descriptors (Figs. S1 and S2), in terms of known generated variation (Figs. S2 and S3), and in terms of expected trends of both temporal and amplitude descriptors (Fig. S3). We motivate these results since MM and BeatProfiler share the same core principle at the base of their algorithms, which consists of quantifying pixel-by-pixel differences in light intensity between consecutive frames as an indirect measurement of cell displacements. Although this approach is advantageous from applicative and computational perspectives, it also relies on the assumption of luminance constancy, which involves considering the microstructures of interest as maintaining the same luminance over the course of the experiment (Szeliski, 2022). This principle can be used as a first approximation; however, it becomes invalid in the presence of focus changes, large or sub-pixel displacements (as those happening at the highest simulated scenarios), and it is clearly violated in our experimental scenario, where the biological models under investigation are exposed to multiple stimuli and variations that alter their appearance over time. Therefore, displacement fields extracted via PIV have been integrated into our system and used in a tailored workflow for contractility analysis in dynamic conditions.

In the absence of a single optimal operating condition, we conditioned the system using multiple electrical stimulations interleaved with drug administration to obtain a broader representation of pharmacological responses in hiPSC-CM models. However, repeated stimulation can introduce physiological bias. Memory effects and contractile fatigue, intrinsic to hiPSC-CM behavior, act as confounders and are difficult to fully separate from drug-induced responses in this setting. To address this issue, we implemented a DMSO-based adjustment procedure (Section 2.4.9). By applying the same stimulation protocol (0.5–2.0 Hz) to the solvent alone, we quantified the average cumulative and memory-related effects associated with the experimental sequence and used them to correct the concentration–response curves.

In the analysis workflow, responses at each pacing frequency were first normalized to their corresponding untreated baseline, then adjusted by subtracting solvent-derived temporal drift, and finally referenced to the onset of each detected beat to reduce slow temporal trends. This strategy compensates for non-stationarity and temporal dependencies in the data, preventing artificial inflation of concentration–response effects and overestimation of statistical significance.

The proposed analysis pipeline does not impose constraints on the

expected beating frequency. All videos were analyzed regardless of whether the hiPSC-CMs strictly followed the imposed conditioning frequency, and no prior selection or exclusion was performed by the experimenter. Rather than selecting samples based on their ability to track pacing, we intentionally diversified the stimulation patterns to induce multiple beating modes and dynamic responses within the same hiPSC-CM population. This strategy was designed to preserve biological heterogeneity and to avoid reducing representativeness and numerosity through pre-selection of fully-paced responses, so deriving a virtual cohort of beating profiles without requiring a high number of biological experiments. In Fig. S4, we show the absence of statistical significance of the treatment effect on the beating frequency, with reference to the control group at $c = 0$ nM, as well as the absence of trends ($p > 0.05$) with increasing concentration values. This result demonstrates the obtained randomization of the multiple dynamic operation modes present within each population (Montgomery, 2017). In fact, even if the biological models might not exhibit frequency tracking at each step of the conditioning strategy, the average of the combined responses at the population level was homogeneous at increasing concentrations, thus minimizing the emergence of biases related to the CMs' beating frequency (a common confounding factor in the interpretation of pharmacological data). Although the potential influence of frequency conditioning on biological samples, also in relation to pacing order and its cumulative effects, have been mitigated, the presence of residual nonlinear effects and sample-specific latencies cannot be entirely ruled out. Therefore, the resulting concentration–response curves should be framed within the context of a dynamic regime.

Modeling of contraction amplitude signals relative to individual beats (Section 2.4.6) was designed to maximize robustness against irregularities and secondary phenomena that could obscure primary drug responses. The Weibull model was selected for its flexibility in capturing the asymmetric shape of PIV-derived beating profiles, enabling independent estimation of contraction onset, amplitude, duration, and waveform asymmetry. This approach provided realistic and stable representations of contraction dynamics. More complex models accounting for aftercontractions, such as bi-exponential formulations, were not considered.

While regularity constraints improved noise robustness and sensitivity to dominant pharmacological effects, second-order phenomena, such as drug-induced arrhythmias, were not explicitly characterized. Approximately 10% of videos were excluded because the algorithm could not detect cyclic mechanical activity or reliably segment contraction beats. This absence of output was likely due to extreme experimental noise (Curci et al., 2026) or weak/non-responding models, potentially influenced by hiPSC-ECs (Brescia et al., 2026). In the absence of a detectable and regular contraction pattern, automatic measurements would lack physiological and quantitative validity. Although missing outputs may reflect pharmacological toxicity, alternative explanations are plausible in high-throughput settings, including cellular immaturity, environmental instability, or methodological limitations. For this reason, when no baseline output was detected, subsequent pharmacological conditions were excluded, as induced changes could not be reliably attributed to the tested compound. Altered amplitude responses were observed at the highest concentrations of ISO and BayK in 2DA, MT, and EHT models; however, confirming toxicity, such as Ca^{2+} overload–related effects (Vassalle and Lin, 2004), would require dedicated descriptors and analysis modules beyond the scope of the present study. These aspects represent a direction for future development.

Notably, the analysis also incorporates samples with lower cell confluence (e.g., the 2DA example shown in the second column of Fig. 2) that would typically be excluded by blind quality-control procedures of human experts due to fewer cell-cell contacts, known to generate altered conduction and increased electrophysiological variability (Hamad et al., 2019; Da Rocha et al., 2017). The presence of low-confluence 2DA samples reduced the signal-to-noise ratio in the derived contraction amplitude estimates, likely due to inherent limitations of the aligned-fiber plate geometry, with average amplitude values approximately one order of magnitude lower than those obtained with the other models (see the colour bar and y-axis values in the last two rows of Fig. 3). This effect was consistent across the different biological samples, frequencies and drugs. Therefore, the lower cell confluence in 2DA indeed led to a higher variability, but this remained acceptable and did not compromise the capacity of the model to quantify drug responses: the ability to extract meaningful information from such datasets represents a key advantage of the method.

5. Conclusion

In this study, we present a fully automated video analysis platform for evaluating drug responses in hiPSC-derived cardiac models based on contractile function. The approach combines drug testing with interleaved electrical stimulation at increasing frequencies, inducing multiple beating modes even when biological replicates are limited. We developed an automated pipeline with normalization and adaptive adjustment strategies to compare across models, improve precision of micron-scale displacement measurements, standardize common contractility indicators, and reproduce expected drug effects. This framework allows dynamic responses at the same drug concentration to be jointly analyzed for concentration–response evaluation. Testing four drugs (plus DMSO) across four biological models, the system, using PIV-derived displacement vectors, provided robust and reliable contractile metrics under dynamic stimulation. Most measured trends were statistically significant and aligned with known drug effects, demonstrating the approach's effectiveness. These results advance high-throughput functional screening of cardiomyocytes for drug testing. While promising, further studies are needed to confirm utility and to develop KIC-based parameters for assessing potential arrhythmogenic effects in candidate compounds.

CRediT authorship contribution statement

Paola Casti: Conceptualization, Data curation, Formal analysis, Investigation, Methodology, Software, Visualization, Writing – original draft, Writing – review & editing. **Marcella Brescia:** Data curation, Investigation, Methodology, Validation, Visualization, Writing – original draft, Writing – review & editing. **Luca Sala:** Data curation, Formal analysis, Methodology, Validation, Writing – review & editing. **Arianna Mencattini:** Data curation, Formal analysis, Software, Visualization, Writing – review & editing. **Massimo Mastrangeli:** Investigation, Methodology, Resources, Validation, Writing – review & editing. **Berend J. van Meer:** Conceptualization, Data curation, Investigation, Methodology, Resources, Validation, Writing – review & editing. **Eugenio Martinelli:** Conceptualization, Funding acquisition, Investigation, Methodology, Project administration, Supervision, Writing – original draft, Writing – review & editing.

Declaration of competing interest

The authors declare that they have no known competing financial interests or personal relationships that could have appeared to influence the work reported in this paper.

Acknowledgements

The hiPSC-CMs and hiPSC-ECs used in this work were kindly provided by Fujifilm CDI. The plates for 2DA alignment were kindly provided by Mimetix.

Appendix A. Supplementary data

Supplementary data to this article can be found online at https://doi.

org/10.1016/j.bios.2026.118717.

Data availability

Data and Matlab codes are available upon request from the corresponding author.

References

Allegaert, K., Simons, S.H.P., Tibboel, D., Krekels, E.H., Knibbe, C.A., van den Anker, J. N., 2017. Eur. J. Pharmaceut. Sci. 109, S27–S31.

Batista, L., Doerr, L., Juhasz, K., Stoelzle-Feix, S., Beckler, M., Bastogne, T., 2019. Mixed-effects modeling for concentration effect profiling in cardiomyocyte contractility assays. J. Pharmacol. Toxicol. Methods 106595.

Bishop, C.M., 2006. Pattern Recognition and Machine Learning. Springer, New York, NY.

Brandão, K.O., van den Brink, L., Miller, D.C., Grandela, C., van Meer, B.J., Mol, M.P.H., de Korte, T., Tertoolen, L.G.J., Mummery, C.L., Sala, L., Verkerk, A.O., Davis, R.P., 2020. Stem Cell Rep. 15, 1127–1139.

Brescia, M., Chatrian, A., Keselman, P., Gallant, J., Paulsson, E.S., Mol, M.P.H., Sjögren, R., Raymond, K., Orlova, V., Barnes, K., Wales, R., Austerjost, J., Olszowy, M.W., Mummery, C.L., van Meer, B.J., Davis, R.P., 2026. Stem Cell Rep. 21.

Caluori, G., Pribyl, J., Pesl, M., Jelinkova, S., Rotrekl, V., Skladal, P., Raiteri, R., 2019. Biosens. Bioelectron. 124–125, 129–135.

Campostrini, G., Windt, L.M., Van Meer, B.J., Bellin, M., Mummery, C.L., 2021. Circ. Res. 128, 775–801.

Chen, S.Y., Qian, H., Wu, Z., Zhu, M.L., 2007. Chinese J. Sensor. Actuator. 20, 1325–1329.

Comes, M.C., Casti, P., Mencattini, A., Di Giuseppe, D., Mermet-Meillon, F., De Ninno, A., Parrini, M.C., Businaro, L., Di Natale, C., Martinelli, E., 2019. Sci. Rep. 9.

Curci, G., Casti, P., Sala, L., Brescia, M., Cascarano, P., Orazio, M.D., Filippi, J., Antonelli, G., Mencattini, A., Mastrangeli, M., Meer, B.J. Van, Martinelli, E., 2026. Expert Syst. Appl. 299, 130302.

Da Rocha, A.M., Campbell, K., Mironov, S., Jiang, J., Mundada, L., Guerrero-Serna, G., Jalife, J., Herron, T.J., 2017. Sci. Rep. 7.

Ewoldt, J.K., DePalma, S.J., Jewett, M.E., Karakan, M.Ç., Lin, Y.M., Mir Hashemian, P., Gao, X., Lou, L., McLellan, M.A., Tabares, J., Ma, M., Salazar Coariti, A.C., He, J., Toussaint, K.C., Bifano, T.G., Ramaswamy, S., White, A.E., Agarwal, A., Lejeune, E., Baker, B.M., Chen, C.S., 2024. Nat. Methods 22.

Fischer, C., Milting, H., Fein, E., Reiser, E., Lu, K., Seidel, T., Schinner, C., Schwarzmayr, T., Schramm, R., Tomasi, R., Husse, B., Cao-Ehlker, X., Pohl, U., Dendorfer, A., 2019. Nat. Commun. 10, 1–12.

Garcia, M.I., Dame, K., Charwat, V., Siemons, B.A., Finsberg, H., Bhardwaj, B., Yokosawa, R., Goswami, I., Bruckner, D., Wall, S.T., Ford, K.A., Healy, K.E., Ribeiro, A.J.S., 2025. Nat. Protoc. 20, 3096–3142.

Giacomelli, E., Bellin, M., Sala, L., van Meer, B.J., Tertoolen, L.G.J., Orlova, V.V., Mummery, C.L., 2017. Dev 144, 1008–1017.

Gintant, G., Kaushik, E.P., Feaster, T., Stoelzle-Feix, S., Kanda, Y., Osada, T., Smith, G., Czysz, K., Kettenhofen, R., Lu, H.R., Cai, B., Shi, H., Herron, T.J., Dang, Q., Burton, F., Pang, L., Traebert, M., Abassi, Y., Pierson, J.B., Blinova, K., 2020. Regul. Toxicol. Pharmacol. 117, 104756.

Guerrelli, D., Pressman, J., Salameh, S., Posnack, N., 2024. Am. J. Physiol. Heart Circ. Physiol. 327, H12–H27.

Hamad, S., Derichsweiler, D., Papadopoulos, S., Nguemo, F., Šarić, T., Sachinidis, A., Brockmeier, K., Hescheler, J., Boukens, B.J., Pfannkuche, K., 2019. Theranostics 9, 7222–7238.

Hamada, C., 2018. J. Toxicol. Pathol. 31, 15–22.

Hinata, Y., Kagawa, Y., Kubo, H., Kato, E., Baba, A., Sasaki, D., Matsuura, K., Sawada, K., Shimizu, T., 2022. J. Pharmacol. Toxicol. Methods 118, 1–11.

Hwang, D.G., Kang, W., Park, S.M., Jang, J., 2024. Biosens. Bioelectron. 260, 116420.

Khan, M., Xu, Y., Hua, S., Johnson, J., Belevych, A., Janssen, P.M.L., Gyorke, S., Guan, J., Angelos, M.G., 2015. PLoS One 10.

Kim, Y., Wang, K., Lock, R.I., Nash, T.R., Fleischer, S., Wang, B.Z., Fine, B.M., Vunjak-Novakovic, G., 2024. IEEE Open J. Eng. Med. Biol. 5, 238–249.

Kirillov, A., Mintun, E., Ravi, N., Mao, H., Rolland, C., Gustafson, L., Xiao, T., Whitehead, S., Berg, A.C., Lo, W.-Y., Dollár, P., Girshick, R., 2023. Segment anything model. In: Proceedings of the EEE/CVF International Conference on Computer Vision. ICCV), pp. 4015–4026.

Knierim, M., Bommer, T., Paulus, M., Riedl, D., Fink, S., Pöppl, A., Reetz, F., Wang, P., Maier, L.S., Voigt, N., Nahrendorf, M., Sossalla, S., Streckfuss-Bömeke, K., Pabel, S., 2024. Am. J. Physiol. Heart Circ. Physiol. 327, H1244–H1254.

Lee, A.P., Reedy, B.J., 1999. Sens. Actuators, B Chem. 60, 35–42.

Marsano, A., Conficconi, C., Lemme, M., Occhetta, P., Gaudiello, E., Votta, E., Cerino, G., Redaelli, A., Rasponi, M., 2016. Lab Chip 16, 599–610.

Martinelli, E., Polese, D., Catini, A., D'Amico, A., Di Natale, C., 2012. Sens. Actuators, B Chem. 161, 534–541.

McKean, R.J., Heister, E., 2017. Mimetix® Electrospun Scaffold, Technology Platforms for 3D Cell Culture.

Mencattini, A., D'Orazio, M., Casti, P., Comes, M.C., Di Giuseppe, D., Antonelli, G., Filippi, J., Corsi, F., Ghibelli, L., Veith, I., Di Natale, C., Parrini, M.C., Martinelli, E., 2023. Commun. Biol. 6.

Mikosch, T., Kallenberg, O., 1998. Foundations of modern probability. J. Am. Stat. Assoc.

Montgomery, D.C., 2017. Design and Analysis of Experiments.

Novelli, G., Spitalieri, P., Murdocca, M., Centanini, E., Sangiuolo, F., 2023. Organoid factory: the recent role of the human induced pluripotent stem cells (hiPSCs) in precision medicine. Front. Cell Dev. Biol.

Rafael, C., Gonzalez, Richard E.W., 2018. Digital Image Processing.

Ribeiro, A.J.S., Ang, Y.S., Fu, J.D., Rivas, R.N., Mohamed, T.M.A., Higgs, G.C., Srivastava, D., Pruitt, B.L., 2015. Proc. Natl. Acad. Sci. U. S. A. 112, 12705–12710.

Richards, D.J., Li, Y., Kerr, C.M., Yao, J., Beeson, G.C., Coyle, R.C., Chen, X., Jia, J., Damon, B., Wilson, R., Starr Hazard, E., Hardiman, G., Menick, D.R., Beeson, C.C., Yao, H., Ye, T., Mei, Y., 2020. Nat. Biomed. Eng. 4, 446–462.

Robinson, A.J., Pérez-Nava, A., Ali, S.C., González-Campos, J.B., Holloway, J.L., Cosgriff-Hernandez, E.M., 2021. Matter 4, 821–844.

Sala, L., Van Meer, B.J., Tertoolen, L.G.J., Bakkers, J., Bellin, M., Davis, R.P., Denning, C., Dieben, M.A.E., Eschenhagen, T., Giacomelli, E., Grandela, C., Hansen, A., Holman, E.R., Jongbloed, M.R.M., Kamel, S.M., Koopman, C.D., Lachaud, Q., Mannhardt, I., Mol, M.P.H., Mosqueira, D., Orlova, V.V., Passier, R., Ribeiro, M.C., Saleem, U., Smith, G.L., Burton, F.L., Mummery, C.L., 2018. Circ. Res. 122, e5–e16.

Sala, L., Ward-van Oostwaard, D., Tertoolen, L.G.J., Mummery, C.L., Bellin, M., 2017. J. Vis. Exp.

Saleem, U., Meer, B.J.V., Katili, P.A., Yusof, N.A.N.M., Mannhardt, I., Garcia, A.K., Tertoolen, L., Korte, T. De, Vlaming, M.L.H., McGlynn, K., Nebel, J., Bahinski, A., Harris, K., Rossman, E., Xu, X., Burton, F.L., Smith, G.L., Clements, P., Mummery, C. L., Eschenhagen, T., Hansen, A., Denning, C., 2020. Toxicol. Sci. 176, 103–123.

Sciacchitano, A., 2019. Meas. Sci. Technol. 30.

Sharma, A., McKeithan, W.L., Serrano, R., Kitani, T., Burridge, P.W., del Álamo, J.C., Mercola, M., Wu, J.C., 2018. Nat. Protoc. 13, 3018–3041.

Smith, A.S.T., Macadangdang, J., Leung, W., Laflamme, M.A., Kim, D.H., 2017. Biotechnol. Adv. 35, 77–94.

Szeliski, R., 2022. Computer Vision: Algorithms and Applications. Springer Nature.

Takahashi, K., Yamanaka, S., 2006. Cell 126, 663–676.

Tertoolen, L.G.J., Braam, S.R., van Meer, B.J., Passier, R., Mummery, C.L., 2018. Biochem. Biophys. Res. Commun. 497, 1135–1141.

Thielicke, W., Sonntag, R., 2021. J. Open Res. Software 9, 1–14.

Thorin, C., Mallem, M.Y., Noireaud, J., Gogny, M., Desfontis, J.-C., 2010. J. Pharm. Pharmacol. 62, 339–345.

van Meer, B.J., Krotenberg, A., Sala, L., Davis, R.P., Eschenhagen, T., Denning, C., Tertoolen, L.G.J., Mummery, C.L., 2019. Nat. Commun. 10, 1–9.

Visone, R., Lozano-Juan, F., Marzorati, S., Rivolta, M.W., Pesenti, E., Redaelli, A., Sassi, R., Rasponi, M., Occhetta, P., 2023. Toxicol. Sci. 191, 47–60.

Windt, L.M., Wiendels, M., Dostanić, M., Bellin, M., Sarro, P.M., Mastrangeli, M., Mummery, C.L., van Meer, B.J., 2023. Biochem. Biophys. Res. Commun. 681, 200–211.

Zeng, H., Balasubramanian, B., Lagrutta, A., Sannajust, F., 2018. J. Pharmacol. Toxicol. Methods 91, 18–26.

Zhang, D., Xiang, Y., Zou, Q., Zhu, K., Hu, N., 2022. Biosens. Bioelectron. 212, 114387.

Zhang, M., D'Aniello, C., Verkerk, A.O., Wrobel, E., Frank, S., Ward-Van Oostwaard, D., Piccini, I., Freund, C., Rao, J., Seebohm, G., Atsma, D.E., Schulze-Bahr, E., Mummery, C.L., Greber, B., Bellin, M., 2014. Proc. Natl. Acad. Sci. U. S. A. 111, E5383–E5392.

Zuiderveld, K., 1994. Graph. Gems, pp. 474–485.